Moving wetting ridges on ultrasoft gels

Hansol Jeon, Youchuang Chao,* and Stefan Karpitschka
Max Planck Insitute for Dynamics and Self-Orgnization, 37077 Göttingen, Germany

(Received 24 January 2023; accepted 28 June 2023; published 24 August 2023)

The surface mechanics of soft solids are important in many natural and technological applications. In this context, static and dynamic wetting of soft polymer gels has emerged as a versatile model system. Recent experimental observations have sparked controversial discussions of the underlying theoretical description, ranging from concentrated elastic forces over strain-dependent solid surface tensions to poroelastic deformations or the capillary extraction of liquid components in the gel. Here we present measurements of the shapes of moving wetting ridges with high spatiotemporal resolution, combining distinct wetting phases (water, FC-70, air) on different ultrasoft PDMS gels (∼100 Pa). Comparing our experimental results to the asymptotic behavior of linear viscoelastocapillary theory in the vicinity of the ridge, we separate reliable measurements from potential resolution artifacts. Remarkably, we find that the commonly used elastocapillary scaling fails to collapse the ridge shapes, but, for small normal forces, yields a viable prediction of the dynamic ridge angles. We demonstrate that neither of the debated theoretical models delivers a quantitative description, while the capillary extraction of an oil skirt appears to be the most promising.

DOI: 10.1103/PhysRevE.108.024611

I. INTRODUCTION

Wetting of soft materials has recently become an intensely studied field of research [1], with rich dynamics [2–7] and applications from biology [8] to soft electronics [9]. Reticulated polymer networks, typically swollen by a liquid fraction of the polymer itself [6,10], are commonly used materials in applications and fundamental research. Typically, these materials are so soft that they can be deformed by the capillarity of their surfaces, i.e., a solid capillary pressure [11]. On long timescales, the liquid fraction in the gel can rearrange, leading to poroelastic relaxation and shape adaptation [6,12]. On small scales, these materials thus behave similar to liquids, dominated by capillary effects. In contrast to liquids, on large scales, these materials behave like solids, resisting permanent loads with a finite storage modulus [13–15]. This dual nature of soft materials poses intriguing scientific questions, especially when it comes to their response to localized loads, in which the capillary and elastic behaviors both contribute.

It is commonly assumed that a three-phase contact line, formed by a liquid meniscus ending on the surface of a soft solid, provides a near-perfect line load, concentrated to molecular scales [1,16,17]. Due to its fundamental and practical relevance, this problem received enormous attention during the last decade [1,18]. Pioneering work showed that the motion of contact lines on soft materials is limited by dissipation in the solid, not the liquid, which is called viscoelastic braking [16,17]. The notion that the local force balance at the three-phase line is of capillary instead of elastic origin was experimentally verified in a series of seminal papers by Style and Park *et al.* [19,20]. Thus, it is believed that this force balance is equivalent to what is known as Neumann's balance for liquid three-phase lines [21].

A purely capillary force balance at a three-phase line is only possible if the three surface tensions fulfill a certain inequality, namely, that none of the surface tensions is larger than the sum of the other two,

$$\gamma_i < \sum_{j \neq i} \gamma_j, \tag{1}$$

where the indices $i, j \in \{\mathrm{LA}, \mathrm{SL}, \mathrm{SA}\}$ indicate the interface between adjacent phases [liquid (L), ambient (A), and solid (S)]. Equivalently, the spreading parameter must be negative for any combination of the three phases. Most of the static and dynamic soft wetting experiments in the past have been conducted for materials where this balance is actually in question, i.e., water/air on cross-linked polydimethylsiloxane (PDMS): The liquid precursor in the soft solid, typically uncross-linked PDMS chains, would spread at the interface of the other two phases rather than forming a stable three-phase line. Still, well-defined angles have been observed experimentally at the three-phase line [19,20,22,23]. Recently, a debate on the contributing forces has emerged, and various mechanisms that could alter the force balance have been proposed, both in static and dynamic situations, including strain-dependent solid surface tensions [15,24–30], surface adaptation [31], concentrated line loads due to nonlinear elastic bulk stresses [32,33], geometric and nonlinear rheological effects [34,35], as well as extraction of free polymer chains from the gel [10,36–39].

*youchuang.chao@ds.mpg.de

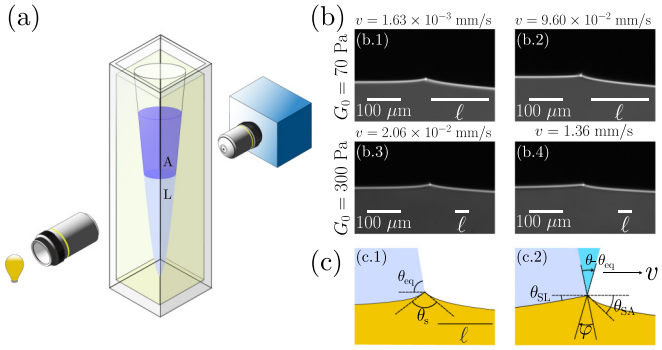

FIG. 1. (a) A cuvette with a parabolic cavity is partially filled with two immiscible phases (bottom, L: FC-70 or water; top, A: water or air). The motion of the meniscus between the two phases and the solid wetting ridge is observed with a shadowgraphy setup. (b) Dynamic wetting ridges under an FC-70/air meniscus. Top: Wetting ridge of a 70 Pa gel traveling with $v = 1.63 \times 10^{-3}$ mm/s (b.1) and $v = 9.60 \times 10^{-2}$ mm/s (b.2). Bottom: Wetting ridge of a 300 Pa gel traveling with $v = 2.06 \times 10^{-2}$ mm/s (b.3) and $v = 1.36$ mm/s (b.4). Right scale bars refer to ℓ, the elastocapillary length of each PDMS gel. (c) Schematic representation of geometry of static (c.1) and moving (c.2) wetting ridges. θ_s is the opening angle of the ridge, and φ indicates rotation of its bisector. θ_{eq} and θ are equilibrium and dynamic liquid contact angles, respectively; $\theta - \theta_{eq}$ the rotation of liquid interface.

Here we revisit this problem, starting with a liquid combination that actually does allow a stable force balance at the three-phase line, even when the liquid precursor to the soft solid, i.e., the uncross-linked substrate material, is considered. In this case, the deformations also remain relatively small, and linear viscoelastocapillary theory is expected to hold near quantitatively. We shadowgraphically visualize wetting ridges at high spatiotemporal resolution (Fig. 1) for various substrate materials and wetting liquids to test the existing scaling relations. With this approach, we show that neither of the former explanation attempts [10,15,25–33,36–39] delivers a consistent description of the observations.

II. EXPERIMENTAL

To obtain the shapes of wetting ridges at high spatiotemporal resolution, we perform shadowgraphy on cylindrical cavities inside blocks of transparent PDMS gels, analogous to previous studies [22,23]. Briefly, the mixed liquid ingredients of the gel formulation are spun at high speed inside a standard optical cuvette while the gel cures. A bubble entrapped in the cuvette is elongated along the rotation axis due to centrifugal forces, forming a stable cylindrical cavity ($R \sim 2$ mm) when the gel is cured. The thickness of the gel layer between the cavity surface and the cuvette inner wall is $h_0 \sim 2$ mm. The surface of the cavity is observed through the gel in grazing incidence, using a long-working distance microscope (Infinitube with Olympus Objective) and a high-speed camera (Phantom VEO 4K). The cavity is illuminated from behind to observe the shadow generated by refraction at the cavity surface [see Fig. 1(a)]. In contrast to earlier experiments where a diffuse illumination was used, here we use a Köhler-type collimated light source, focused into the imaging plane by a 5x Mitutoyo microscopy objective. Refraction of light at the cavity surface casts a shadow, while reflection of the collimated light at the gel surface creates a narrow bright line that enhances the visualization of the surface profile. We estimate the resolution of this imaging setup to ∼2 μm, but exclude any data closer than ∼4 μm to the ridge tip from the analysis, to avoid picking up optical artifacts. Surface profiles are extracted from the shadowgraphs by first calculating the mean intensity gradient in Gaussian-weighted neighborhoods (standard deviation ∼3 px) and determining local maxima of the magnitude of the gradient along the direction of the gradient. We determine the slopes at the resolution limit (∼4 μm) by fitting empirical functions to the profile data and compare these slopes to theory to extract the rotation of the ridge tip φ and the solid opening angle θ_s [Fig. 1(c), see Appendix A for more information on the data analysis]. In addition to the ridge profile, we obtain an estimate of the dynamic liquid contact angle relative to the undeformed substrate, by monitoring the shadow of the liquid meniscus through the cavity [Fig. 1(c)]. At the center of the cavity, distortion from the lensing effect of the cavity is minimal and the meniscus position can be determined precisely. Since the capillary length and the ridge location are known, and the capillary number remains very small, the liquid angle at the ridge can be determined.

As gels, we use three different formulations. For a very soft gel, we use Dow Corning CY52-276, mixing components A and B in a mass ratio of 1.3:1, to obtain zero-frequency storage modulus $G_0 \sim 70$ Pa. For slightly stiffer gels, we use custom formulations, based on a vinyl-end-functionalized PDMS prepolymer (DMS-V31, Gelest) and two different methylhydrosiloxane-dimethylsiloxane copolymers (HMS-053 and HMS-082, Gelest) as cross-linker, and a platinum-complex catalyst (SIP6831.2, Gelest); The preparation procedure was analogous to Ref. [25]. We first prepare two stock mixtures, base and catalyst (component A) and base and cross-linker (component B), respectively, in proportions that the desired ratio of base polymer to cross-linker in the final gel formulation is achieved by mixing components A and B at a 9:1 mass ratio. Then, the second gel with $G_0 \sim 300$ Pa is obtained with 97.30 wt% of DMS-V31 and 2.70 wt% of HMS-053, estimating a nonstoichiometric molar ratio of vinyl to hydride groups of 3.8. Fig. 2 shows the rheometric spectra of the two gels, where the viscoelastic rheology can be fitted by the Chasset-Thirion constitutional model, $\mu(\omega) = G'(\omega) + i\,G''(\omega) = G_0[1 + (i\,\omega\tau)^n]$, with zero-frequency storage modulus G_0, timescale τ, and rheological exponent n [17]. A third gel with $G_0 \sim 340$ Pa is obtained with 96.78 wt% of DMS-V31 and 3.22 wt% of HMS-082, estimating a molar ratio of vinyl to hydride groups of 2.1. This gel is intentionally prepared with a different cross-linker molecule and a different deviation from the stoichiometric ratio of the functional groups, but a modulus comparable to the previous one. We repeat all experiments on the third gel, finding nearly identical profiles as for the 300 Pa gel. Thus in the following, we will focus exclusively on the 70 Pa and 300 Pa gels. All cavities are stored for a few days prior to use, to achieve stationary gel and surface states [40].

The wetting ridge is formed on the inside of the cavity by the meniscus of a liquid that fills the bottom half of the cavity, leaving the upper half exposed to ambient air. As

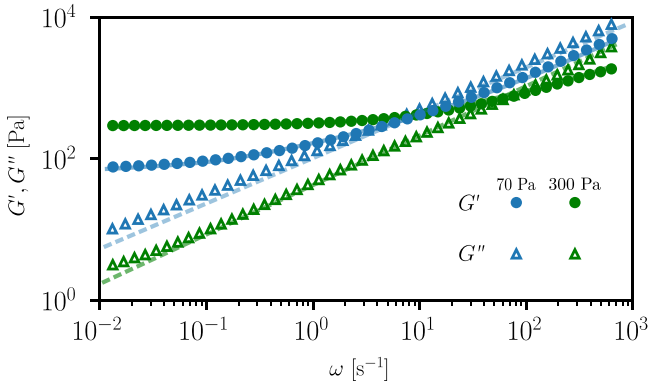

FIG. 2. Rheometric spectra of the two main gels used (symbols), together with fits of the Chasset-Thirion constitutional model (lines). Blue: Dow Corning CY52-276A/B, mixed 1.3:1 ($G_0 \sim 70$ Pa). Green: Gelest DMS-V31 + HMS-053 ($G_0 \sim 300$ Pa). Closed symbols: G'. Open symbols: G''.

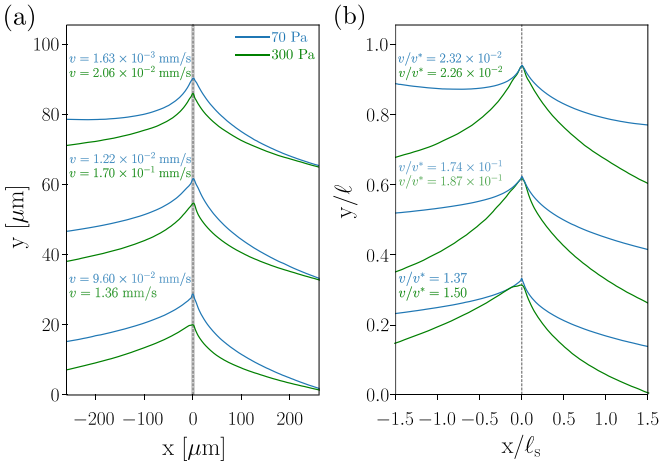

FIG. 3. Wetting ridge profiles extracted from the shadowgraphic images. Blue curves: Profiles of gel with $G_0 \sim 70$ Pa; green curves: profiles of gel with $G_0 \sim 300$ Pa. (a) Profiles in physical units. A vertical offset has been added to arrange the profiles conveniently. (b) Profiles scaled with ℓ in y, and ℓ_s in x.

liquids, we use a fluorinated oil, FC-70 (Sigma) and Milli-Q water (resistivity 18.1 MΩcm). We also perform experiments where the FC-70 meniscus was covered with Milli-Q water, to obtain an additional set of solid and liquid surface tensions. To measure interfacial tensions of liquid surfaces, the pendant drop method (OCA20, DataPhysics Instruments) is used. For notational convenience and in most situations, we use the index L to denote the liquid phase that is in the bottom of the cavity, and A for the ambient, upper phase, which can be air or water [Fig. 1(a)].

The motion of the meniscus is induced by injecting liquid into the bottom phase of the cavity using a Nemesys syringe pump with a Hamilton gas tight syringe, connected to a needle that sticks through the liquid meniscus. Importantly, these syringe pumps generate virtually no stick-slip motion in their actuators [41], allowing for truly stationary motion of the menisci. All experiments are preformed at room temperature, $\sim 22 \pm 1\,^\circ$C.

III. WETTING RIDGE PROFILES

Figure 3(a) shows the surface profiles of moving wetting ridges induced by an FC-70/air meniscus on two gels, with $G_0 \sim 70$ Pa (blue) and $G_0 \sim 300$ Pa (green), and for various velocities, increasing from top to bottom. The profiles have been shifted along the vertical axis for a convenient arrangement. We define the elastocapillary length using the normal force that the liquid interface exerts at equilibrium, $\ell = \gamma \sin\theta_{eq}/G_0$, where γ is the liquid surface tension and θ_{eq} is Young's angle, as a scale for the ridge height. These elastocapillary lengths are also indicated as scale bars in Fig. 1(b). According to linear theory [42], the horizontal length scale $\ell_s = \Upsilon_s/G_0$ involves the solid surface tension Υ_s, which is not known *a priori*, typically different on either side of the ridge, and may, in addition, depend on the surface strain. To obtain a suitable estimate for a mean ℓ_s, we extract the solid opening angle θ_s (see Fig. 1) from the profiles and calculate an effective Υ_s [43] from the vertical force balance, $2\Upsilon_s \sin((\pi - \theta_s)/2) = \gamma \sin\theta_{eq}$. The profiles, scaled with ℓ and ℓ_s on vertical and horizontal axes, respectively, are shown in Fig. 3(b), again shifted vertically to align the tips of the ridges. Note that we apply the different physical contact line velocities of the two different gels, so they become comparable after being scaled with the corresponding characteristic velocity, $v^* = \Upsilon_s/(G_0\tau)$ [22,42]. Apparently, the profile shapes collapse near the ridge tip for dimensionless velocities $v/v^* < 1$. For dimensionless speeds $v/v^* > 1$, a small deviation near the tips can be seen. However, this deviation is in the range where optical artifacts due to the corner cannot safely be excluded anymore [see Fig. 3(b)]. Quite remarkably though, despite their collapse at small $|x|$, the scaled profiles deviate significantly already for $|x| \sim 0.2\ell_s$. If the regular viscoelastocapillary theory [17,42] would apply, the scaled profiles should collapse up to $|x| \sim \ell_s$.

A sharp fold at the surface of an elastic half space, as induced by a contact line, exhibits a regular strain energy density but generates a logarithmic pressure singularity, both in finite strain and in linear theory [44,45]. For a wetting ridge, the surfaces next to the fold are free and subject to solid capillarity. Thus, the pressure singularity manifests itself in a logarithmic divergence of the curvature of the solid surface, which has been shown in finite strain numerical simulations and experiments [45,46]. Note that the slopes and thus the contact angles remain regular because the logarithmic singularity is integrable.

Now two questions arise: (i) Can the ridge angles be determined faithfully from our experiments, i.e., do our experiments resolve scales on which the slopes have substantially converged to the angles at the three-phase line? (ii) Does viscoelastic dissipation in moving wetting ridges generate some kind of singularity that might enter the force balance or even render Neumann angles ill-defined, as observed theoretically for Kelvin-Voigt substrates [7,42]?

To address these questions, we first analyze the solid shape in the vicinity of the contact line in the framework of linear viscoelasticity, solving for the slope $h'(x)$ of a wetting ridge moving at velocity v. We scale x by ℓ_s, h' by ℓ, and v by

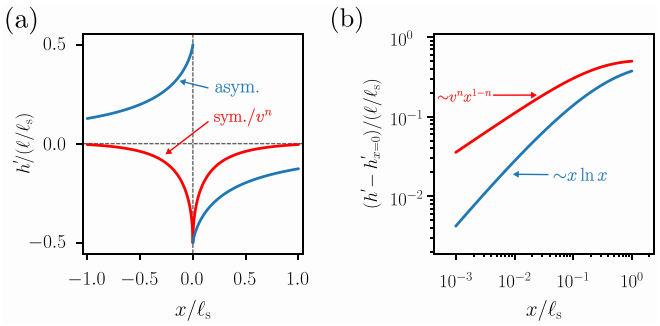

FIG. 4. Asymptotic surface slopes of moving wetting ridges for small x and v, with $n = 1/2$: (a) linear scale and (b) double-logarithmic scale after subtracting the slope at $x = 0$. The asymmetric component (blue) corresponds to a static ridge and is independent of v to the leading order. The symmetric component (red) scales as v^n and converges much slower to the limiting value at the contact line.

v^*. The Fourier transform of the slope is readily obtained following Ref. [42],

$$\widehat{h'}(q) = \frac{-i\,q}{\mu(v\,q)/\chi(q) + q^2}, \tag{2}$$

where q is the wave number in units of ℓ_s^{-1}, and $\chi(q)$ is the Green's function for the geometry of the solid. The solution in real space $h'(x)$ is obtained by Fourier inversion of $\widehat{h'}(q)$. Here we are primarily interested in the properties of the solution near the tip of the ridge, well below the elastocapillary length, while the outer length, i.e., the wall thickness of the soft cavity, is much larger than ℓ_s. Thus, the elastic behavior can locally be approximated by an elastic half space, i.e., $\chi(q) \sim (2|q|)^{-1}$.

To analyze the shape near the tip, we expand Eq. (2) into real and imaginary parts, and those separately for small v:

$$\widehat{h'}(q) = \frac{-i\,q}{2|q| + q^2} - v^n \frac{|q|^n \sin\frac{n\pi}{2}}{2 + 2|q| + q^2/2} + O(v^{n+1}). \tag{3}$$

Physically, the small-v expansion corresponds to approximating the symmetric component of the ridge shape by the static solution because the leading-order consequence of dissipation is the emergence of an antisymmetric component in the shape, close to the tip. The imaginary part in Eq. (3) resembles the static solution and carries a slope discontinuity at $x = 0$, encoded in the $\sim q^{-1}$ asymptote for large q. The real part introduces a symmetric component $\sim v^n$ to the slope due to viscoelastic dissipation.

Equation (3) can be inverted analytically to obtain a lengthy expression, plotted in Fig. 4, which shows the following asymptotic behavior at small x,

$$h'(x) \sim -\frac{\mathrm{sign}x}{2} - \frac{2x\,(\ln 2|x| + \gamma_E - 1)}{\pi} - v^n\left(2^{n-1} n \sec\frac{n\pi}{2} + \frac{2\Gamma(n-1)\sin^2\frac{n\pi}{2}}{\pi}|x|^{1-n}\right), \tag{4}$$

where $\gamma_E = 0.5772\ldots$ is Euler's constant. The first line of Eq. (4) resembles the asymmetric component of the slope [blue lines in Fig. 4(a)], which is identical to the static solution. Its slope discontinuity at $x = 0$ represents the Neumann balance. Such sharp surface fold introduces a log-singular elastic stress in its vicinity which, by elastocapillarity, is translated into a log-singular surface curvature. The second line represents the symmetric component of the slope [red lines in Fig. 4(a)], which is caused by dissipation and scales as v^n. The constant component corresponds to a rotation of the ridge tip, which had already been derived earlier [42]. In addition, one can identify an algebraic divergence of stress and curvature, $h'' \sim x^{-n}$. This singularity is also integrable across the contact line, does not generate a line force, and the Neumann angles remain well-defined. Recent numerical simulations showed that the behavior of the viscoelastic stress is qualitatively maintained for finite strain viscoelasticity when using an equivalent relaxation law [47].

TABLE I. Surface tensions in mN/m of various liquids against each other. For PDMS, we measure the surface tensions of the non-cross-linked base polymer. For water/air, we consider a PDMS-cloaked interface, using the value from Ref. [38]. The other interfacial tensions are measured by the pendant drop method. Measurement errors are ±0.5 mN/m except for water/air, which varies ∼ ± 1 mN/m [38].

	Water	FC-70	PDMS
Air	64.0	18.0	19.8
Water		50.6	42.4
FC-70			6.7

Figure 4(b) shows the deviation of the dissipative (symmetric, red) and static (asymmetric, blue) slope components from their values at the contact line, scaling the symmetric component also with v^n, on logarithmic scales. The dissipative component of stress and thus surface curvature diverges much stronger than the elastic component, such that the corresponding components of the slope converges much slower to its value at the contact line. At a distance $\sim\ell_s/10$, the static component of the slopes deviates by ∼20% from the value at the contact line [$h'(x = \pm 0, v = 0) = \mp 1/2$], while the corresponding deviation of the viscoelastic component remains much stronger unless the contact line speed is much smaller than the elastocapillary speed. Thus, in both experiments and simulations, resolutions well beyond $\sim\ell_s/10$ are required to correctly resolve the solid contact angles.

To estimate the actual surface slopes at the contact line and thus θ_{SL} and θ_{SA} [see Fig. 1(c)] from the profiles shown in Fig. 3, we use the asymptotic result of the linear theory, fitting the prefactor, to obtain parameters that describe the ridge shape well below the elastocapillary length, noting that finite strains might yield quantitatively different results. For the low surface tension fluid system (FC-70/air), the capillary traction is small compared to the surface tension of the fluid/PDMS gel interface (see Table I), leading to small surface slopes and thus small strains. Therefore, comparing experiments to linear viscoelastic theory appears reasonable. For larger strains, the character of the elastic and dissipative stress singularities remains unchanged as far as geometric nonlinearity is considered, only the prefactor changes [47]

and the comparison is still meaningful (see Appendix A). For the softer gel, the resolution limit is around $\ell_s/40$, for which a residual deviation is expected to be small. For the stiffer gel, however, we achieve only $\ell_s/10$, and nonlinear effects, especially for the viscoelastic component, might still show significant deviations.

IV. QUASISTATIC RIDGE ANGLES

Instead of measuring truly static ridges, we here extrapolate the solid angles of moving wetting ridges for $v \to 0$. This has two advantages: On the one hand, we avoid the ambiguity of a possible residual velocity, which can be as small as 1 nm/s; on the other hand, we minimize excessive poroelastic deformation, which occurs on long timescales, most noticably for wetting ridges that have been residing at the same location for extended periods of time, although poroelastic relaxation will still be present [6,48]. For FC-70/air on gels, extrapolating our measurements of $\theta_{\mathrm{PDMS/FC70}}$ and $\theta_{\mathrm{PDMS/air}}$ for $v \to 0$, we obtain $\theta_{\mathrm{PDMS/FC70}} \sim \theta_{\mathrm{PDMS/air}} \sim 17°$, independent (within the errors $\sim \pm 1°$) of the stiffness of the gel. These values match almost perfectly to those reported on static FC-70 droplets on PDMS gels in air, using confocal microscopy to localize surface-attached beads [19]. We also test FC-70/water and water/air on all our gels. For FC-70/water, we obtain $\theta_{\mathrm{PDMS/FC70}} \sim \theta_{\mathrm{PDMS/water}} \sim 34°$, again independent of the gel stiffness. For water/air, we obtain $\theta_{\mathrm{PDMS/water}} \sim \theta_{\mathrm{PDMS/air}} \sim 50°$ for the 70 Pa gel, and $\theta_{\mathrm{PDMS/water}} \sim \theta_{\mathrm{PDMS/air}} \sim 45°$ for the 300 Pa gel. The angles of the last case are most likely suffering from a resolution problem, since the true nonlinear stress might be quantitatively different from the linear model. Also, x-ray microscopy experiments yielded different values for this case [20]. Remarkably, however, we always find symmetric ridge tips for $v \to 0$, independent of the gel or the liquid combination.

Since cross-linking of PDMS leaves the molecular interactions of the PDMS chains largely unchanged, it is instructive to compare the observed angles to the Neumann angles against liquid PDMS. By employing a Neumann construction, using the surface tensions of the liquids against each other and the liquid PDMS base polymer (see Table I), namely, $\theta_s = \pi - \theta_{\mathrm{PDMS/FC70}} - \theta_{\mathrm{PDMS/air}}$, for FC-70/air on PDMS, one would expect $\theta_s \sim 115°$. The validity of this Neumann construction is confirmed in a direct measurement of the angle in the liquid PDMS phase $\sim 115°$, using an air bubble at the interface between bulk FC-70 and liquid PDMS (Fig. 5). This value is significantly smaller than our measurement for wetting on cross-linked PDMS, which gives $\theta_s \sim 146°$ for FC-70/air on all cross-linked gels.

Since bulk elasticity does not generate line forces at sharp folds [44,45,49], the deviation must be caused by altered surface tensions or other surface-bound phenomena. Several hypotheses have been proposed to explain this deviation in the Neumann angles between liquid and cross-linked PDMS: (i) the cross-linking reaction alters the surface tension [50], (ii) strain-dependent solid surface tension [25], and (iii) extraction of liquid PDMS precursor from the network into a wetting skirt that, in addition, may [36,38] or may not [6,31,37] cloak the liquid-vapor surface and lower its effective tension [51].

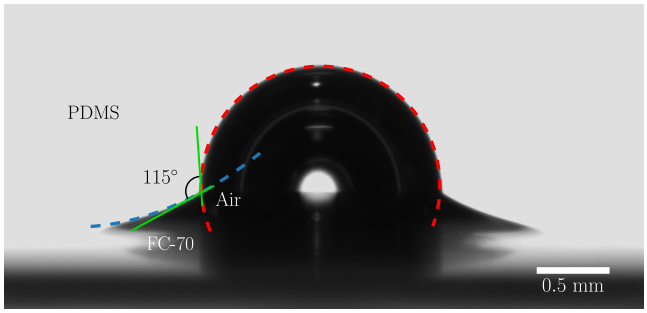

FIG. 5. An air bubble trapped at the interface of liquid PDMS (top) and FC-70 (bottom). The Neumann angle in the PDMS phase is extracted from the bubble (red dashed line) and meniscus (blue dashed line) contours.

For case (i), one would expect that the surface tension of cross-linked PDMS is different from liquid PDMS but depends only on the liquid it is in contact with. In particular, it should not be affected by the strain at the ridge tip. We apply three different liquid/ambient interface combinations, namely, FC-70/air, FC-70/water, and water/air, with different interfacial tensions, measuring the solid opening angle θ_s for each combination, i.e., $\theta_s \sim 146°$, $112°$, and $80°$, respectively (see Table II). Here, the values of θ_s are calculated by $\theta_s = \pi - \theta_{\mathrm{SL}} - \theta_{\mathrm{SA}}$, where θ_{SL} and θ_{SA} are obtained by extrapolating the measured slopes on the two sides of the ridge with the asymptotes from linear theory, Eq. (4), fitting the prefactors to match the experimentally measured slopes at $\sim 4\,\mu$m away from the tip. For each θ_s, the surface stress can be calculated from the Neumann balance, using the measured θ_{eq}, θ_{SL}, θ_{SA}, and γ. Thus, we obtained two Υ_s values for each PDMS/fluid interface (rows in Table II), corresponding to a different third phase and thus different θ_s. We find that, under different θ_s, the obtained Υ_s values differ significantly for the each liquid/ambient interface combination (see Table II), which is also well beyond any reasonable experimental error estimate, so we arrive at hypothesis (ii).

For case (ii), we may use the Neumann construction preformed above to estimate the solid surface stresses. For the case of FC-70/air on PDMS, the value we obtain matches well with previous reports [19]. Solid surface tension is assumed to depend primarily on the surface dilational strain, which can be estimated from the inclination of the surface: $\epsilon_s \sim \sqrt{1 + (h')^2} - 1 \sim h'$. This means a decreasing θ_s corresponds to an increasing strain: the wetting ridge gets sharper, i.e., the deformation (of the originally flat surface, $\theta_s = 180°$) increases. From Table II, we find that for PDMS/air and

TABLE II. Surface tension Υ_s in mN/m, obtained from the Neumann construction under various liquid combinations on top of cross-linked PDMS gels. Typical uncertainties are ± 1 mN/m, except for $\theta_s \sim 80°$, where a large systematic error cannot be ruled out.

	$\theta_s \sim 146°$	$\theta_s \sim 112°$	$\theta_s \sim 80°$
PDMS/air	28.0		21.5
PDMS/water		53.6	56.7
PDMS/FC-70	14.3	10.5	

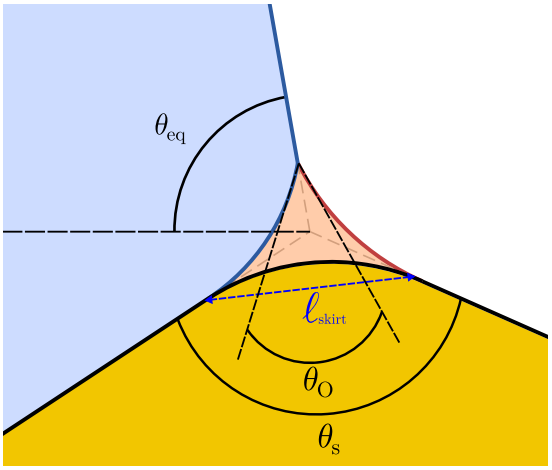

FIG. 6. Extended Neumann construction in the presence of a liquid skirt (light red), presumably extracted from the soft gel (yellow). Contact angles between the oil and the gel are assumed to vanish. For cloaking of the liquid interface with oil, the Neumann angle θ_O would vanish.

PDMS/FC-70 interfaces, the surface tensions decrease with increasing strain. Note that the values (56.7 mN/m) on the last column for water/air on PDMS ($\theta_s \sim 80\,^\circ$) probably suffer from a large systematic error, leading to underestimated $\Upsilon_{PDMS/water}$ and $\Upsilon_{PDMS/air}$. Park *et al.* reported $\Upsilon_{PDMS/water}$ ~16 mN/m and $\Upsilon_{PDMS/air}$ ~59 mN/m, without taking into account cloaking [20]. Correcting their values for PDMS-cloaked water, we would obtain $\Upsilon_{PDMS/water}$ ~14 mN/m and $\Upsilon_{PDMS/air}$ ~52 mN/m. Observing surface tensions that decrease with decreasing solid angle contradicts the assumption of a strain-dependent solid surface tension since measurements with externally stretched surfaces showed that surface stress increases with strain [25,45].

In case (iii), the three-phase line is no longer located at the solid surface. Instead, an oil skirt [37,39] with a negative Laplace pressure p_{skirt} transmits the normal force of the liquid/liquid or liquid/air interface, $\gamma \sin\theta$, onto the solid, distributed over a width ℓ_{skirt}: $p_{skirt} = \gamma \sin\theta/\ell_{skirt}$. Figure 6 shows a sketch of this wetting configuration. The distributed pressure can straightforwardly be implemented into linear viscoelastocapillary theory from Ref. [42] to estimate the surface slopes of the gel, using a normal traction (in physical units) $t_n = \gamma \sin\theta \cdot \Theta(\ell_{skirt}/2 - |x|)$, with $\Theta(x)$ the Heaviside theta function. The expression for the surface slopes, Eq. (3), is then multiplied with the Fourier transform of the traction profile,

$$\widehat{h'}(q) = \frac{-i\,\frac{\ell_s}{\ell_{skirt}}\,\sin\frac{q\,\ell_{skirt}}{\ell_s}}{\mu(v\,q)/\chi(q) + q^2}, \tag{5}$$

The surface slopes are then calculated by numerical Fourier inversion. Given the small ridge surface slopes $\theta_{PDMS/FC70} \sim \theta_{PDMS/air}$ ~17 ° observed for FC-70/air on PDMS gels, this model should be near-quantitatively accurate. To obtain $\theta_s \sim 146^\circ$, a skirt with $\ell_{skirt} \sim 0.86\ell_s$ is required, corresponding to 150 μm and 41 μm for ~70 Pa and ~300 Pa gels, respectively. In the light of recent direct visualizations of oil skirts for static [37], and moving [39] contact lines on artificially swollen networks, this estimate appears unreasonably large.

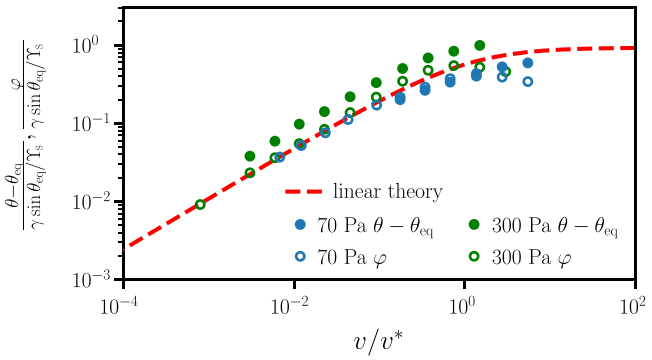

FIG. 7. Rotation of the liquid interface ($\theta - \theta_{eq}$, filled symbols) and the bisector of the wetting ridge (φ, open symbols), scaled by the aspect ratio $\ell/\ell_s = \gamma \sin\theta_{eq}/\Upsilon_s$ as a function of velocity v scaled by the characteristic velocity v^*. The red dashed line shows the result of linear viscoelastocapillary theory.

Prior to extraction, the free oil phase in the PDMS gel has to be advected toward the contact line, which is indeed predicted by nonlinear poroelasticity theory [52]. Since the refractive index of the oil and network are expected to be well-matched, poroelastic deformations remain invisible in our experiments, i.e., showing up as bright as and thus indistinguishable from the gel, despite their significant size. Poroelastic swelling would further reduce the effective modulus of the gel at the tip. On the one hand, this would reduce the skirt size required to obtain the observed θ_s. On the other hand, such enhanced swelling would show up in a deviation of the typical ridge shape.

This is indeed observed in Fig. 3(b): The scaled profiles for different gel stiffnesses deviate significantly from each other for $|x| \gtrsim 0.2\ell_s$. The elastocapillary model would predict a good match between the profiles up to $|x| \sim \ell_s$ because the outer length, i.e., the gel thickness, is much larger than ℓ_s in both cases and does not impact the local shapes. Instead, we find a closer match between the shapes in physical units. Given that the surface tensions are identical for both cases, this indicates that the zero-frequency shear modulus G_0 is not a good scaling parameter here. Whether or not the observed ridge shapes can be described by, e.g., linear poroelasticity [48] remains to be evaluated.

V. DYNAMIC RIDGE ANGLES

Figure 7 shows the rotation of the liquid interface, $\theta - \theta_{eq}$ (filled symbols) and of the ridge bisector, φ (open symbols: experiments; red dashed line: linear viscoelastocapillary theory), for FC-70/air on our softer (~70 Pa, blue) and stiffer (~300 Pa, green) gels. The rotations have been scaled by the typical aspect ratio, i.e., ℓ/ℓ_s, and the velocity by the characteristic velocity v^*. For the 70 Pa gel (blue), we find a good agreement between the measured liquid and solid rotation, as well as the prediction from linear theory. Since the wetting ridges under FC-70/air menisci exhibit rather small surface slopes ($\theta_{PDMS/FC70} \sim \theta_{PDMS/air}$ ~17 °), one may expect that linear theory could deliver reasonable results here. For the 300 Pa gel (green), however, we find a deviation between the liquid rotation and the solid rotation, while the latter collapses

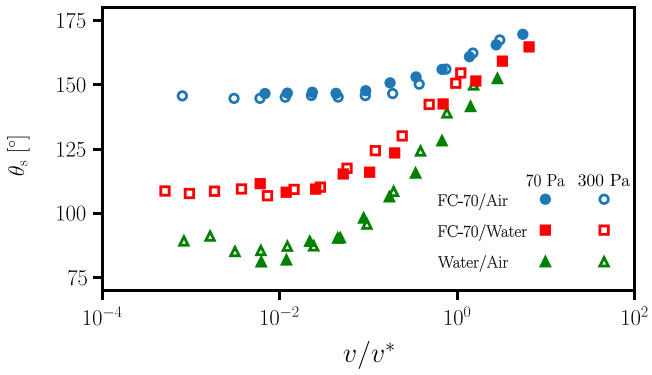

FIG. 8. Solid opening angle θ_s as a function of velocity v, scaled by the characteristic velocity v^*. For small speeds, the angle remains constant, increasing only at large speeds. Data for soft and stiff gels collapses in this scaling. Larger γ, i.e., smaller θ_s, leads to an earlier increase of θ_s.

onto the data from the soft gel and the model. Possibly, the velocity-dependent component of the ridge slopes has not been extracted with sufficient resolution, and thus the rotation is underestimated. The liquid angle does not suffer from such resolution limit since the capillary number remains very small and the meniscus shape is not expected to show significant deviations from its static shape. Thus, the dissipation generated by the 300 Pa gel appears to be increased relative to the 70 Pa gel or the theory. Finally, under the assumption of a poroelastic relaxation and/or an extracted oil skirt, the match between theory and the softer gel would be surprising. In this case, poroelastic dissipation or the dissipation in the skirt would have to be taken into account as well. If the loss modulus of the free oil phase was similar to the cross-linked gel, however, such a behavior could be rationalized.

Figure 8 shows the solid opening angle θ_s for all liquid combinations and the two gels, with velocity v scaled by the elastocapillary velocity v^*. We notice that for small scaled velocities v/v^*, θ_s remains constant. For large v/v^*, θ_s increases. The larger the liquid surface tension γ, i.e., the larger the normal traction and the smaller θ_s, the earlier the detected θ_s increases with v, which points to a nonlinear effect that is triggered by the surface strain. The curves for different gels, however, collapse perfectly in the case of same liquid-fluid combinations, indicating that the time scale τ of the rheological model correctly describes the dynamics. Previously, the velocity-dependent increase of θ_s has been interpreted by a dynamical increase of the surface stresses, which yielded a quantitative explanation for the transition to stick-slip motion [22]. Given the asymptotic behavior of the slopes in the linear theory outlined above, resolution artifacts would, however, be expected to manifest in a similar way. Yet, then the stiffer gel should be more prone to these artifacts, and the collapse suggests this is not the case. Invoking again the hypotheses of poroelastic relaxation and/or extraction of an oil skirt by the contact line, as well as taking into account the noncollapse of the ridge profiles, the storage modulus in the ridge-tip region should be smaller than the independently measured G_0, and the length scales no longer depend on it. Further, the increase in θ_s can be reproduced in the linear model with a distributed traction. On the scale of the skirt, viscoelasticity significantly contributes to the force balance, and the increase of the moduli with frequency then leads to an increase of the solid angle.

VI. CONCLUSION

We have shown that both the static and the dynamic angles at the tip of a wetting ridge cannot quantitatively be described by standard linear viscoelastocapillary theory. The solid angle θ_s is typically much larger than expected from the Neumann balance for liquid PDMS. Neither linear nor finite strain bulk elasticity can generate line forces at sharp surface folds [44,45] that could contribute to the Neumann balance. It remains open though, whether a cusplike singularity of the profile, possibly combined with strain-stiffening constitutional laws, would generate a stronger stress singularity with a nonzero integral. For the case primarily studied here, FC-70/air on PDMS, such a singular profile is not expected. From the Neumann deconstruction of the ridge tip, we derive surface stresses that depend on θ_s. We find that the stresses decrease with θ_s, which seemingly contradicts measurements of the surface stress in response to an external strain [25,27]. We also find that surface profiles on gels of different stiffness do not collapse, apart from a region very close ($|x| \lesssim 0.2\ell_s$) to the ridge tip, when scaled with the elastocapillary length. This indicates that the zero-frequency storage modulus G_0 is not a good parameter for the scaling behavior of the ridge profile, and some critical processes could be missing in current theories. For instance, the size scale deviation of the wetting ridges could be explained by a model that combines viscoelastic dissipation [17,42] with dynamic poroelasticity [48,52–54]. Due to solvent aspiration toward the ridge tip [52,53], the effective stiffness near the tip decreases, and a spatially varying poroelastocapillary length would be required to describe the ridge shape. The observed decreasing Υ_s with increasing strain might be caused by the noninert nature of PDMS surfaces, reacting to the liquid on top of it, e.g., hydrolysis reactions of PDMS [31,55]. Furthermore, reticulated polymer networks are inherently multiscale, and a systematic derivation of continuum equations from microscopic models might lead to nonlocal constitutive relations. The size of the nonlocal kernel could further depend on swelling, since swelling impacts the distance between cross-links [50,56]. Including these features in theoretical models of static and dynamic soft wetting might finally deliver a consistent theoretical understanding of the experimental observations [10,15,25–33,36–39].

Despite these discrepancies for the shapes and the static properties of wetting ridges, we find a rather good agreement between the measured rotation and the linear theory, at least for the softer gel where we can exclude significant experimental errors due to resolution limitations. This suggests that the elastocapillary velocity, $v^* = \Upsilon_s/(G_0\tau)$, remains identical upon poroelastic swelling of the tip, i.e., $G_0\,\tau$ remains almost constant, which can also be observed when the cross-linking degree is tuned (see Appendix B for more information). Further, this points out that, should indeed poroelastic relaxation or an oil skirt be responsible for the observed shapes, then these regions should exhibit a similar elastocapillary veloc-

ity v^* as the underlying gel. The measurement of the liquid angle indicates that the shadowgraphy misses a dissipative rotation of the ridge that is localized within the last ∼4 μm. This could be due to finite strain effects or high-frequency components in the loss modulus that are not detected in oscillatory rheometry. Unfortunately, with our current experimental setup, higher spatiotemporal resolution is beyond reach. Phase contrast x-ray microscopy at a synchrotron facility [20,57] could reveal the ridge properties at increased resolution and possibly identify regions of excess dissipative stress.

ACKNOWLEDGMENTS

We thank L. Hauer, D. Vollmer and R. Seemann for helpful discussions on oil skirt extraction, and M. H. Essink and J. H. Snoeijer on strain dependent surface tensions and finite strain viscoelasticity. S.K. and H.J. acknowledge funding from the German research foundation (DFG, Project No. KA4747/2-1). Y.C. acknowledges support through an Alexander von Humboldt Fellowship.

APPENDIX A: DATA ANALYSIS NEAR THE RIDGE TIP

In the following, we describe how we obtain the profile slopes near the ridge tip at the optical resolution limit and how we apply our theory to extract two key parameters from the experiments, φ and θ_s. Due to the asymmetry of the wetting ridge, especially at a high velocity [see Fig. 1(b)], we closely follow our previous work [22,23] and fit each side of the contact line with a separate, empirical shape, but exclude profile data within ∼4 μm from the tip, where optical artifacts are observed. For the right-hand side profile [in contact with phase A, Fig. 1(b)], we use a generic logarithmic function $h(x) = a_2 + b_2 \log(c_2 + x)$, regularizing the near-field singularity by the offset c_2. For the left-hand side profile [in contact with phase L, Fig. 1(b)], where the profile becomes nonmonotonic for faster speeds, we use a third-order polynomial function, $h(x) = a_1 + b_1 x + c_1 x^2 + d_1 x^3$, to allow for a nonconstant curvature as observed in the experiments. Figure 9 shows the comparison between the fitting curves and the raw data points near the wetting tip, including the slow and fast velocities for ∼70 Pa and ∼300 Pa gels in panels (a), (b) and (c), (d), respectively. The wavy structure of the tip profiles, i.e., the deviations of the extracted profile points from the fit curves very near the tip (∼2 μm), particularly in the case of high contact-line velocity, is most likely due to optical artifacts. We note that these deviations are quite random and not systematic, which probably comes from the limited resolution of our setup and the fine details of the tip geometry that changes with speed and contact line position, so it appears safest to exclude these data. From these fitted profiles, we extract the slopes at the optical resolution limit, i.e., ∼4 μm away from the tip. By matching the slopes to the asymptotic expressions, Eq. (4) from our linear theory, we obtain the ridge parameters φ and θ_s.

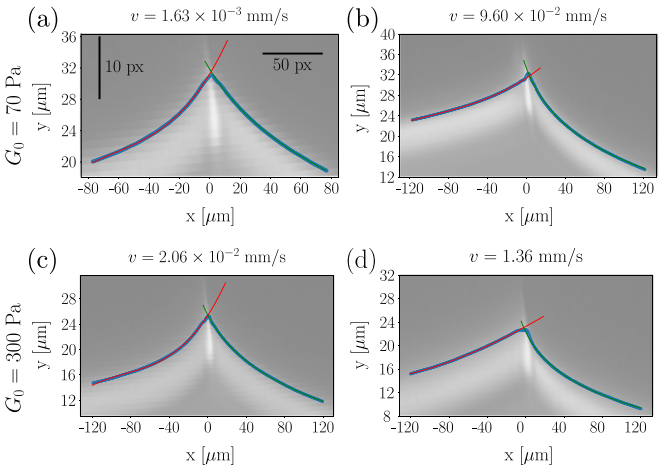

FIG. 9. Comparison between the shadowgraphic images (grayscale, reduced contrast), the extracted profile data (teal circles) and the fitting curves (red and green) near the tip of the wetting ridge for (a), (b) ∼70 Pa gel and (c), (d) ∼300 Pa gel. Tip artifacts are visible as a bright spot near the ridge tip. The outer range of the curve fitting is typically between 80 and 120 μm, and profile data within ∼4 μm from the tip are excluded.

APPENDIX B: RHEOLOGICAL PROPERTIES VS STOICHIOMETRIC MISMATCH

Figure 10(a) shows the zero-frequency storage mudulus G_0 as a function of molar ratio between vinyl and hydride groups, i.e., $n_{vinyl}/n_{hydride}$. We test two different ingredient combinations obtained from Gelest Inc., namely, DMS-V31 + HMS-053 and DMS-V31 + HMS-082. The base polymer (DMS-V31) is functionalized on both ends with vinyl groups, while each cross-linker molecule carries ∼15.2 (HMS-053) or 6.4 (HMS-082) hydride groups on average, according to manufacturer specifications. Figure 10(b) shows the corresponding relaxation time τ as a function of G_0. When adjusting G_0 by the cross-linking degree, τ changes approximately inversely, so that $G_0\,\tau$ remains nearly constant. Thus the elastocapillary velocity, $v^* = \Upsilon_s/(G_0\tau)$ remains rather

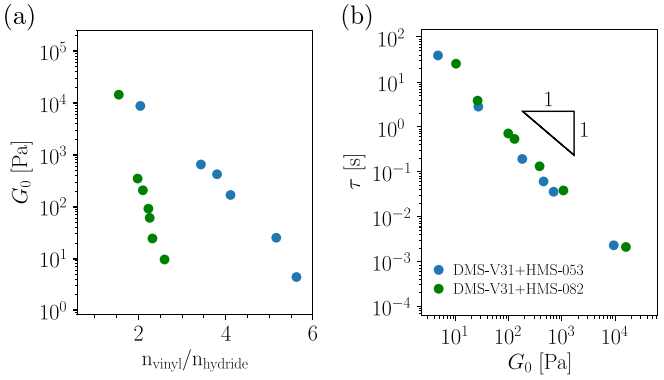

FIG. 10. Plots of rheological parameters: (a) Zero-frequency storage mudulus G_0 as a function of molar ratio between vinyl groups (end functionalization of the base polymer) and hydride groups (functional groups on the cross-linker), i.e., $n_{vinyl}/n_{hydride}$. (b) The corresponding relaxation time τ as a function of G_0.

similar when the cross-linking density is changed. Poroelastic swelling, as it occurs for the ridge tip [52], also reduces the cross-linking density, and would thus change τ and G_0 simultaneously, presumably in a similar way.

[1] B. Andreotti and J. H. Snoeijer, Statics and dynamics of soft wetting, Annu. Rev. Fluid Mech. **52**, 285 (2020).

[2] T. Kajiya, A. Daerr, T. Narita, L. Royon, F. Lequeux, and L. Limat, Advancing liquid contact line on visco-elastic gel substrates: Stick-slip vs. continuous motions, Soft Matter **9**, 454 (2013).

[3] R. W. Style, Y. Che, S. J. Park, B. M. Weon, J. H. Je, C. Hyland, G. K. German, M. P. Power, L. A. Wilen, J. S. Wettlaufer, and E. R. Dufresne, Patterning droplets with durotaxis, Proc. Natl. Acad. Sci. U.S.A. **110**, 12541 (2013).

[4] S. Karpitschka, A. Pandey, L. A. Lubbers, J. H. Weijs, L. Botto, S. Das, B. Andreotti, and J. H. Snoeijer, Liquid drops attract or repel by the inverted Cheerios effect, Proc. Natl. Acad. Sci. U.S.A. **113**, 7403 (2016).

[5] A. Pandey, S. Karpitschka, L. A. Lubbers, J. H. Weijs, L. Botto, S. Das, B. Andreotti, and J. H. Snoeijer, Dynamical theory of the inverted Cheerios effect, Soft Matter **13**, 6000 (2017).

[6] Q. Xu, L. A. Wilen, K. E. Jensen, R. W. Style, and E. R. Dufresne, Viscoelastic and Poroelastic Relaxations of Soft Solid Surfaces, Phys. Rev. Lett. **125**, 238002 (2020).

[7] D. Mokbel, S. Aland, and S. Karpitschka, Stick-slip contact line motion on Kelvin-Voigt model substrates, Europhys. Lett. **139**, 33002 (2022).

[8] C. Pérez-González, R. Alert, C. Blanch-Mercader, M. Gómez-González, T. Kolodziej, E. Bazellieres, J. Casademunt, and X. Trepat, Active wetting of epithelial tissues, Nat. Phys. **15**, 79 (2019).

[9] J. A. Rogers, T. Someya, and Y. Huang, Materials and mechanics for stretchable electronics, Science **327**, 1603 (2010).

[10] J. D. Glover, C. E. McLaughlin, M. K. McFarland, and J. T. Pham, Extracting uncrosslinked material from low modulus sylgard 184 and the effect on mechanical properties, J. Polym. Sci. **58**, 343 (2020).

[11] S. Mora, T. Phou, J.-M. Fromental, L. M. Pismen, and Y. Pomeau, Capillarity Driven Instability of a Soft Solid, Phys. Rev. Lett. **105**, 214301 (2010).

[12] M. G. Hennessy, A. Münch, and B. Wagner, Phase separation in swelling and deswelling hydrogels with a free boundary, Phys. Rev. E **101**, 032501 (2020).

[13] L. A. Lubbers, J. H. Weijs, L. Botto, S. Das, B. Andreotti, and J. H. Snoeijer, Drops on soft solids: Free energy and double transition of contact angles, J. Fluid Mech. **747**, R1 (2014).

[14] B. Zhao, E. Bonaccurso, G. K. Auernhammer, and L. Chen, Elasticity-to-capillarity transition in soft substrate deformation, Nano Lett. **21**, 10361 (2021).

[15] C. Henkel, J. H. Snoeijer, and U. Thiele, Gradient-dynamics model for liquid drops on elastic substrates, Soft Matter **17**, 10359 (2021).

[16] A. Carré, J.-C. Gastel, and M. E. R. Shanahan, Viscoelastic effects in the spreading of liquids, Nature **379**, 432 (1996).

[17] D. Long, A. Ajdari, and L. Leibler, Static and dynamic wetting properties of thin rubber films, Langmuir **12**, 5221 (1996).

[18] R. W. Style, A. Jagota, C.-Y. Hui, and E. R. Dufresne, Elastocapillarity: Surface tension and the mechanics of soft solids, Annu. Rev. Condens. Matter Phys. **8**, 99 (2017).

[19] R. W. Style, R. Boltyanskiy, Y. Che, J. S. Wettlaufer, L. A. Wilen, and E. R. Dufresne, Universal Deformation of Soft Substrates Near a Contact Line and the Direct Measurement of Solid Surface Stresses, Phys. Rev. Lett. **110**, 066103 (2013).

[20] S. J. Park, B. M. Weon, J. S. Lee, J. Lee, J. Kim, and J. H. Je, Visualization of asymmetric wetting ridges on soft solids with x-ray microscopy, Nat. Commun. **5**, 4369 (2014).

[21] J. H. Snoeijer, E. Rolley, and B. Andreotti, Paradox of Contact Angle Selection on Stretched Soft Solids, Phys. Rev. Lett. **121**, 068003 (2018).

[22] M. van Gorcum, B. Andreotti, J. H. Snoeijer, and S. Karpitschka, Dynamic Solid Surface Tension Causes Droplet Pinning and Depinning, Phys. Rev. Lett. **121**, 208003 (2018).

[23] M. van Gorcum, S. Karpitschka, B. Andreotti, and J. H. Snoeijer, Spreading on viscoelastic solids: Are contact angles selected by Neumann's law? Soft Matter **16**, 1306 (2020).

[24] R. Shuttleworth, The surface tension of solids, Proc. Phys. Soc. London, Sect. A **63**, 444 (1950).

[25] Q. Xu, K. E. Jensen, R. Boltyanskiy, R. Sarfati, R. W. Style, and E. R. Dufresne, Direct measurement of strain-dependent solid surface stress, Nat. Commun. **8**, 555 (2017).

[26] R. D. Schulman, M. Trejo, T. Salez, E. Raphaël, and K. Dalnoki-Veress, Surface energy of strained amorphous solids, Nat. Commun. **9**, 982 (2018).

[27] Q. Xu, R. W. Style, and E. R. Dufresne, Surface elastic constants of a soft solid, Soft Matter **14**, 916 (2018).

[28] J. Y. Kim, S. Heyden, D. Gerber, N. Bain, E. R. Dufresne, and R. W. Style, Measuring Surface Tensions of Soft Solids with Huge Contact-Angle Hysteresis, Phys. Rev. X **11**, 031004 (2021).

[29] K. Smith-Mannschott, Q. Xu, S. Heyden, N. Bain, J. H. Snoeijer, E. R. Dufresne, and R. W. Style, Droplets Sit and Slide Anisotropically on Soft, Stretched Substrates, Phys. Rev. Lett. **126**, 158004 (2021).

[30] S. Heyden, N. Bain, Q. Xu, R. W. Style, and E. R. Dufresne, Contact lines on stretched soft solids: Modelling anisotropic surface stresses, Proc. Math. Phys. Eng. Sci. **477**, 20200673 (2021).

[31] W. S. Y. Wong, L. Hauer, A. Naga, A. Kaltbeitzel, P. Baumli, R. Berger, M. D'Acunzi, D. Vollmer, and H.-J. Butt, Adaptive wetting of polydimethylsiloxane, Langmuir **36**, 7236 (2020).

[32] J. Dervaux, M. Roché, and L. Limat, Nonlinear theory of wetting on deformable substrates, Soft Matter **16**, 5157 (2020).

[33] R. Masurel, M. Roché, L. Limat, I. Ionescu, and J. Dervaux, Elastocapillary Ridge as a Noninteger Disclination, Phys. Rev. Lett. **122**, 248004 (2019).

[34] M. Zhao, J. Dervaux, T. Narita, F. Lequeux, L. Limat, and M. Roché, Geometrical control of dissipation during the spreading of liquids on soft solids, Proc. Natl. Acad. Sci. U.S.A. **115**, 1748 (2018).

[35] H. K. Khattak, S. Karpitschka, J. H. Snoeijer, and K. Dalnoki-Veress, Direct force measurement of microscopic droplets pulled along soft surfaces, Nat. Commun. **13**, 4436 (2022).

[36] A. Hourlier-Fargette, A. Antkowiak, A. Chateauminois, and S. Neukirch, Role of uncrosslinked chains in droplets

dynamics on silicone elastomers, Soft Matter **13**, 3484 (2017).

[37] Z. Cai, A. Skabeev, S. Morozova, and J. T. Pham, Fluid separation and network deformation in wetting of soft and swollen surfaces, Commun. Mater. **2**, 21 (2021).

[38] C. S. Sharma, A. Milionis, A. Naga, C. W. E. Lam, G. Rodriguez, M. F. D. Ponte, V. Negri, H. Raoul, M. D'Acunzi, H.-J. Butt, D. Vollmer, and D. Poulikakos, Enhanced condensation on soft materials through bulk lubricant infusion, Adv. Funct. Mater. **32**, 2109633 (2022).

[39] L. Hauer, Z. Cai, A. Skabeev, D. Vollmer, and J. T. Pham, Phase Separation in Wetting Ridges of Sliding Drops on Soft and Swollen Surfaces, Phys. Rev. Lett. **130**, 058205 (2023).

[40] J. D. Glover, X. Yang, R. Long, and J. T. Pham, Creasing in microscale, soft static friction, Nat. Commun. **14**, 2362 (2023).

[41] Z. Li, S. Y. Mak, A. Sauret, and H. C. Shum, Syringe-pump-induced fluctuation in all-aqueous microfluidic system implications for flow rate accuracy, Lab Chip **14**, 744 (2014).

[42] S. Karpitschka, S. Das, M. van Gorcum, H. Perrin, B. Andreotti, and J. H. Snoeijer, Droplets move over viscoelastic substrates by surfing a ridge, Nat. Commun. **6**, 7891 (2015).

[43] Actually, there are two different surface stresses for L and A, so as an effective value we use the homogeneous surface stress that would lead to the same θ_s.

[44] M. Singh and A. C. Pipkin, Note on Ericksen's problem, Z. Angew. Math. Phys. **16**, 706 (1965).

[45] A. Pandey, B. Andreotti, S. Karpitschka, G. J. van Zwieten, E. H. van Brummelen, and J. H. Snoeijer, Singular Nature of the Elastocapillary Ridge, Phys. Rev. X **10**, 031067 (2020).

[46] M. A. J. van Limbeek, M. H. Essink, A. Pandey, J. H. Snoeijer, and S. Karpitschka, Pinning-Induced Folding-Unfolding Asymmetry in Adhesive Creases, Phys. Rev. Lett. **127**, 028001 (2021).

[47] M. H. Essink, Soft contact: From wetting to adhesion, Ph.D. thesis, Universiteit Twente, 2022.

[48] C. Kopecz-Muller, V. Bertin, E. Raphaël, J. D. McGraw, and T. Salez, Mechanical response of a thick poroelastic gel in contactless colloidal-probe rheology, Proc. Math. Phys. Eng. Sci. **479**, 20220832 (2023).

[49] S. Karpitschka, S. Das, M. van Gorcum, H. Perrin, B. Andreotti, and J. H. Snoeijer, Soft wetting: Models based on energy dissipation or on force balance are equivalent, Proc. Natl. Acad. Sci. U.S.A. **115**, E7233 (2018).

[50] W. Zhao, J. Zhou, H. Hu, C. Xu, and Q. Xu, The role of crosslinking density in surface stress and surface energy of soft solids, Soft Matter **18**, 507 (2022).

[51] A cloaked surface is comprised of two interfaces (PDMS/water and PDMS/air) in very close proximity, so the "effective" tension describes the combined action of both interfaces.

[52] M. M. Flapper, A. Pandey, M. H. Essink, E. H. van Brummelen, S. Karpitschka, and J. H. Snoeijer, Reversal of Solvent Migration in Poroelastic Folds, Phys. Rev. Lett. **130**, 228201 (2023).

[53] M. Zhao, F. Lequeux, T. Narita, M. Roché, L. Limat, and J. Dervaux, Growth and relaxation of a ridge on a soft poroelastic substrate, Soft Matter **14**, 61 (2018).

[54] J. D. Berman, M. Randeria, R. W. Style, Q. Xu, J. R. Nichols, A. J. Duncan, M. Loewenberg, E. R. Dufresne, and K. E. Jensen, Singular dynamics in the failure of soft adhesive contacts, Soft Matter **15**, 1327 (2019).

[55] G. Ducom, B. Laubie, A. Ohannessian, C. Chottier, P. Germain, and V. Chatain, Hydrolysis of polydimethylsiloxane fluids in controlled aqueous solutions, Water Sci. Technol. **68**, 813 (2013).

[56] Y. Jiang, L. Li, and Y. Hu, A physically-based nonlocal strain gradient theory for crosslinked polymers, Int. J. Mech. Sci. **245**, 108094 (2023).

[57] S. J. Park, J. B. Bostwick, V. D. Andrade, and J. H. Je, Self-spreading of the wetting ridge during stick-slip on a viscoelastic surface, Soft Matter **13**, 8331 (2017).